Available online at www.sciencedirect.com
ScienceDirect
Journal of Computational Physics 217 (2006) 759–781
JOURNAL OF COMPUTATIONAL PHYSICS
www.elsevier.com/locate/jcp

Finite-difference method for incompressible Navier–Stokes equations in arbitrary orthogonal curvilinear coordinates

Nikolay Nikitin

Institute of Mechanics of Moscow State University, Laboratory of General Aeromechanics, 117192, Michurinsky pr. 1, Moscow, Russian Federation

Received 15 September 2005; received in revised form 19 January 2006; accepted 23 January 2006
Available online 13 March 2006

Abstract

A finite-difference method for solving three-dimensional time-dependent incompressible Navier–Stokes equations in arbitrary curvilinear orthogonal coordinates is presented. The method is oriented on turbulent flow simulations and consists of a second-order central difference approximation in space and a third-order semi-implicit Runge–Kutta scheme for time advancement. Spatial discretization retains some important properties of the Navier–Stokes equations, including energy conservation by the nonlinear and pressure-gradient terms. Numerical tests cover Cartesian, cylindrical-polar, spherical, cylindrical elliptic and cylindrical bipolar coordinate systems. Both laminar and turbulent flows are considered demonstrating reasonable accuracy and stability of the method.

PACS: 47.11.+j

Keywords: Navier–Stokes equations; Turbulent flows; Curvilinear orthogonal coordinates; Central differences; Energy conservation; Semi-implicit Runge–Kutta method

1. Introduction

During the last decades, direct numerical simulations (DNS) have been recognized as a powerful and reliable tool for studying the basic physics of turbulence. Numerous examples showed that results obtained by DNS are in excellent agreement with experimental findings, if the latter are reliable [1]. In some respects DNS-based studies are even more advantageous than experimental ones since far more detailed information on the flow field structure can be achieved. Another, perhaps even more important advantage is that DNS allows exposure of new important physical mechanisms of turbulence production and self-sustainability via so-called *unphysical experiment* [2,3].

However, one major difficulty that arises with a numerical investigation of turbulent flow is the presence of a vast, continuous range of relevant scales of motion which must be correctly resolved by numerical

E-mail addresses: nta@rsuh.ru, nvnikitin@mail.ru.

0021-9991/$ - see front matter
doi:10.1016/j.jcp.2006.01.036

simulation. DNS of turbulent wall-bounded flows, for example, require order $Re^{21/8}$ storage and order $Re^{7/2}$ work to resolve dynamically significant velocity fluctuations at large Reynolds numbers [4]. That is why most DNS-based works are restricted to relatively low Reynolds number and focus on simple-geometry flows for which accurate and efficient numerical algorithms exist. For wall-bounded turbulent flows, the majority of successful DNS-based studies dealt with the simplest geometry cases such as a plane channel, a flat plate boundary layer, a circular pipe and some other similar cases [5–9].

The turbulent flows listed above are one-dimensional in the mean. Numerical investigations of multi-dimensional (in the mean) turbulent flows are rather more restricted. Among them are the flows in noncircular straight duct of square [10–12], elliptic [13], and eccentric annular [14] cross-sections. For several other examples see [4] and the references therein.

For simple computational domains the generation of the computational grid is trivial; the simulations of flows in industrially relevant geometries, on the other hand, are extremely complicated and time consuming since the shape of the domain must include the wetted surface of the geometry of interest. During the past three decades numerical grid generation has become an essential part of computational fluid dynamics. For mathematical aspects of numerical grid generation and applications see [15,16] and the references therein. An alternative numerical procedure that can handle the geometric complexity is an immersed boundary method (IBM). Nikitin and Yakhot [13] have used IBM for DNS of turbulent flow in elliptic ducts. IBM allows the reduction of complex-geometry simulation to simple-geometry one (for more information on IBM see [17,18]). Possessing a number of remarkable features, IBM is inconvenient, however, for the detailed flow analysis in the vicinity of solid curvilinear boundaries, i.e., in the most interesting flow region from the dynamical point of view.

Sometimes the geometry of the flow permits an introduction of curvilinear orthogonal coordinates, so that the flow boundaries coincide with the coordinate surfaces. In these cases near-wall regions may be resolved in detail on a simple computational mesh. An extensive literature is devoted to the different aspects of numerical solution of the Navier–Stokes equations (NSE) in curvilinear orthogonal coordinates: cylindrical [7,19–28], spherical [29,30], and bipolar [14,31]. Of particular interest are conservation properties of numerical schemes and treatment of coordinate singularities.

This paper presents a method for finite-difference approximation of the incompressible NSE in arbitrary curvilinear orthogonal coordinates. The corresponding discrete equations retain a number of important local and integral properties of the NSE. In particular, the energy conservation property, which means that the nonlinear and pressure-gradient terms do not produce kinetic energy of the motion but only redistribute it among different flow regions, is held identically by the discretized equations.

Spatial discretization of the incompressible NSE with sufficiently fine resolution leads to stiff problems and requires implicit methods for time advancement. Fully implicit methods produce a set of nonlinear coupled equations for the flow variables on the new time level, and are usually prohibitively costly for long-term calculations, such as turbulent flow simulations, for example. Semi-implicit methods, in which only a part of the Navier–Stokes operator is treated implicitly, present a reasonable compromise for this class of flows. In fact, the majority of direct and large eddy simulations to date have used semi-implicit time-advancement methods. For wall-bounded flows only the linear viscous term of the NSE is usually treated implicitly and the corresponding set of linear equations is solved effectively with the help of an approximate factorization technique.

One of the popular schemes was proposed in [32]. It consists of a second-order-explicit Adams–Bashforth method for the convective terms and a second-order-implicit Crank–Nicolson for the viscous term. The Adams–Bashforth method, as well as first- and second-order accurate Runge–Kutta methods, is unconditionally unstable for a pure convection equation. However, the instability is weak, and the method usually works for CFL numbers less than 1.0 in the presence of a viscous term. Third-order accurate Runge–Kutta methods seem more suitable for convective terms because of their stability. Slightly different semi-implicit schemes, based on a third-order accurate low-storage Runge–Kutta method were presented in [22,33,34]. The scheme with similar properties but incorporating an algorithm of time-step size control [21] was proposed in [9]. All these are the three-step schemes, which require three times more operations to advance on a new time level compared with the scheme of [32]. However, due to high accuracy and stability they are often preferable compared with the Adams–Bashforth based schemes.

The mentioned Runge–Kutta based schemes use second-order accurate implicit methods for the viscous term (or other linear terms which are treated implicitly), thus, their overall accuracy is second-order in time.

Apparently, it is impossible to achieve a third-order accuracy within a classical three-step semi-implicit Runge–Kutta method, each step of which consists of the three substeps: (a) evaluation of the convective and viscous terms of the NSE for a given velocity field, (b) solution of a linear system, connected with the implicit terms, and (c) solution of a Poisson equation for the pressure (or pseudo-pressure). A pure third-order accurate semi-implicit Runge–Kutta scheme for NSE was developed in [35]. The higher order of accuracy is achieved due to one extra substep (b). Thus, the scheme may be referred as a $3\frac{1}{3}$-step scheme. Note, that among the three substeps, solution of the Poisson equation is usually the most time consuming substep except in the case of a spectral spatial discretization. On the contrary, evaluation of the nonlinear convective terms in substep (a) is the most expensive for spectral methods. Regarding substep (b), it is a relatively inexpensive substep both in spectral and finite-difference methods when using approximate factorization technique. Thus, the overall overhead of the scheme is similar to that of the classical one. The scheme is supplied with a built-in local accuracy estimation and time-step control algorithm [21], which proved itself to be convenient and efficient, especially for flows with variations in characteristic time scales.

One of the difficulties in constructing high-order-accurate implicit time integration schemes for the NSE is the so called *pressure problem*. It arises because the equations for the velocity and the pressure are a coupled system with the incompressibility condition. Nearly all numerical schemes for solving NSE in terms of primitive variables use a *fractional step approach* in which the auxiliary velocity field is at first computed by ignoring the incompressibility constraint and then projected onto a divergence-free field. The determination of boundary conditions for the auxiliary velocity field and pressure related quantities has been a subject of considerable discussion in the literature over many years (see [36] and references therein). The scheme of [35] is constructed in terms of the spatially discretized NSE. Following this approach [37,38] no boundary conditions for the auxiliary velocity fields are needed. Only the final velocity field at each complete time step of the scheme satisfies the incompressibility condition exactly, while the velocities on the intermediate time levels are divergence-free only to within a certain truncation error. Such a trick leads to a relatively simple solution to the pressure problem while retaining a desired order of accuracy.

The paper is organized as follows. Governing equations for incompressible flow in curvilinear orthogonal coordinates are presented in Section 2. The derivation of the scalar form of the NSE using the metric stretching factors is discussed there as well. The numerical method is described in detail in Section 3. Spatial discretization and the features of the discretized NSE are discussed in Section 3.1. Section 3.2 is devoted to the derivation of the pressure equation. The time-advancement scheme is presented in Section 3.3. A method of viscous term decomposition with the aim of using the approximate factorization procedure is proposed in Section 3.4. A set of numerical tests covering laminar and turbulent flows in Cartesian, cylindrical, spherical, elliptical and bipolar coordinates is collected in Section 4. A summary is given in Section 5. Numerical evidence of the third-order accuracy of the proposed time-integrating scheme and discussion of energy conservation property of the method are presented in appendices. The examples given in the paper are restricted to interior flows. Formulation of the far-field boundary conditions peculiar to unbounded flows is beyond the scope of the paper. However, as soon as the boundary conditions are properly formulated the proposed scheme may by applied to unbounded flows as well.

2. Formulation and governing equations

Consider a flow of viscous incompressible fluid governed by the Navier–Stokes and continuity equations:

$$\frac{\partial \mathbf{u}}{\partial t} = \mathbf{u} \times \boldsymbol{\omega} - \nu \operatorname{curl} \boldsymbol{\omega} - \operatorname{grad} p, \tag{1}$$

$$\operatorname{div} \mathbf{u} = 0. \tag{2}$$

Here, $\mathbf{u}(t,\mathbf{x})$ is the velocity, $p(t,\mathbf{x})$ is the full kinematic pressure (i.e., sum of the pressure and the velocity head $\rho|\mathbf{u}|^2/2$, divided by the fluid density ρ), ν is the fluid viscosity, and $\boldsymbol{\omega}(t,\mathbf{x})$ is the vorticity

$$\boldsymbol{\omega} = \operatorname{curl} \mathbf{u}. \tag{3}$$

Eq. (1) is derived from the more conventional form of the NSE using the vector identities

$$-(\mathbf{u}\cdot\nabla)\mathbf{u} \equiv \mathbf{u}\times\operatorname{curl}\mathbf{u} - \operatorname{grad}|\mathbf{u}|^2/2, \quad \nabla^2\mathbf{u} \equiv \operatorname{grad}\operatorname{div}\mathbf{u} - \operatorname{curl}\operatorname{curl}\mathbf{u}$$

and with (2) and (3) taken into account.

We assume that the flow domain is D with the boundary Γ, and the boundary conditions are given in the form

$$\mathbf{u}(t,\mathbf{x}) = \mathbf{u}_b(t,\mathbf{x}) \quad \text{at } \mathbf{x}\in\Gamma. \tag{4}$$

Several other kinds of boundary conditions, as well as the conditions at the coordinate singularity points will be considered below in the test examples. Concerning the boundary velocity $\mathbf{u}_b$, to be consistent with the incompressibility the following condition must be satisfied:

$$\int_\Gamma \mathbf{u}_b\cdot\mathbf{n}\,d\Gamma = 0, \tag{5}$$

where $\mathbf{n}$ is the normal vector.

In this paper, we consider the case when D is a rectangular domain in some orthogonal curvilinear coordinates (x_1,x_2,x_3) connected with the Cartesian coordinates (x,y,z) by the relations

$$x = x(x_1,x_2,x_3), \quad y = y(x_1,x_2,x_3), \quad z = z(x_1,x_2,x_3). \tag{6}$$

Vector operators in curvilinear orthogonal coordinates: gradient of a scalar field ϕ, divergence and curl of a vector field $\mathbf{a} = (a_1,a_2,a_3)$ are defined as follows:

$$\operatorname{grad}\phi = \left(\frac{1}{h_1}\frac{\partial\phi}{\partial x_1}, \frac{1}{h_2}\frac{\partial\phi}{\partial x_2}, \frac{1}{h_3}\frac{\partial\phi}{\partial x_3}\right), \tag{7}$$

$$\operatorname{div}\mathbf{a} = \frac{1}{h}\left[\frac{\partial}{\partial x_1}\left(\frac{ha_1}{h_1}\right) + \frac{\partial}{\partial x_2}\left(\frac{ha_2}{h_2}\right) + \frac{\partial}{\partial x_3}\left(\frac{ha_3}{h_3}\right)\right], \tag{8}$$

$$\operatorname{curl}\mathbf{a} = \left(\frac{h_1}{h}\left[\frac{\partial h_3a_3}{\partial x_2} - \frac{\partial h_2a_2}{\partial x_3}\right], \frac{h_2}{h}\left[\frac{\partial h_1a_1}{\partial x_3} - \frac{\partial h_3a_3}{\partial x_1}\right], \frac{h_3}{h}\left[\frac{\partial h_2a_2}{\partial x_1} - \frac{\partial h_1a_1}{\partial x_2}\right]\right). \tag{9}$$

Here, h_1,h_2,h_3 are the *metric stretching factors*

$$h_k = \sqrt{\left(\frac{\partial x}{\partial x_k}\right)^2 + \left(\frac{\partial y}{\partial x_k}\right)^2 + \left(\frac{\partial z}{\partial x_k}\right)^2}, \quad k = 1,2,3 \tag{10}$$

and $h = h_1h_2h_3$.

Finally, taking into account, that by definition of vector product

$$\mathbf{u}\times\boldsymbol{\omega} = (u_2\omega_3 - u_3\omega_2, u_3\omega_1 - u_1\omega_3, u_1\omega_2 - u_2\omega_1),$$

the vector equations (1)–(3) may be written in a scalar form.

3. Numerical method

3.1. Spatial discretization

Let x_k^s and x_k^e be the start- and the end-points of the flow domain in the kth direction. The interval $[x_k^s, x_k^e]$ is divided into N_k equal segments of the size Δ_k, each. Thus, the flow domain is divided into $N_1\times N_2\times N_3$ equal rectangular volumes. Note, that in the physical space the size of the mesh cell is $d_1\times d_2\times d_3 \approx \Delta_1h_1\times\Delta_2h_2\times\Delta_3h_3$ and varies from point to point. A staggered mesh layout [39] is used to represent the mesh functions corresponding to different continuous unknown functions: pressure, three velocity components, and three vorticity components. As usual, the pressure-nodes are in the geometrical centers of the cells. The u_k velocity-nodes are at the centers of the cell's faces, shifted from the pressure-nodes at the half-cell distance towards the kth direction. The ω_k vorticity-nodes are at the centers of the cell's edges directed along the kth direction. The sketch of the velocity- and vorticity-nodes layout is shown in Fig. 1.

All spatial derivatives in the expressions for the vector operations are replaced by central differences approximating them with a second order of accuracy:

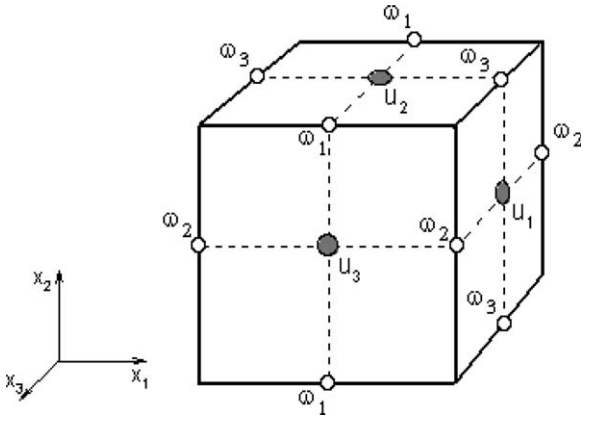

Fig. 1. Sketch of the velocity- and vorticity-nodes layout. Only the forefront cell faces are shown for clearness.

$$\frac{\delta f(x_k)}{\delta x_k} = \frac{f(x_k + \Delta_k/2) - f(x_k - \Delta_k/2)}{\Delta_k} = \frac{\partial f(x_k)}{\partial x_k} + \mathrm{O}(\Delta_k^2). \tag{11}$$

Location of the vorticity-nodes at the cell's edges is dictated by the expressions for the vorticity components following from (9). For example, $\omega_1 = \frac{h_1}{h}\left(\frac{\partial h_3 u_3}{\partial x_2} - \frac{\partial h_2 u_2}{\partial x_3}\right)$. And, since ω_1-nodes are at half way between two adjacent u_3-nodes along x_2 direction and at the same time are at half way between two adjacent u_2-nodes along x_3 direction, the central-difference approximation of the ω_1 expression is straightforward. Similar considerations are applicable to ω_2 and ω_3. Furthermore, one can see from Fig. 1 that each velocity node is surrounded by four vorticity nodes at the same cell face. Thus, components of the viscous term of the NSE in the form $\nu \operatorname{curl} \boldsymbol{\omega}$ can be easily approximated by central differences using the vorticity components in the adjacent points.

Different multipliers in the nonlinear terms of the NSE correspond to different nodes, therefore a cell-averaging operation is applied where it is necessary:

$$\bar{f}^k(x_k) = \frac{f(x_k - \Delta_k/2) + f(x_k + \Delta_k/2)}{2} = f(x_k) + \mathrm{O}(\Delta_k^2). \tag{12}$$

Finally, the discretized NSE are written in the following form:

$$\frac{\partial u_1}{\partial t} = \frac{h_1}{h}\left(\overline{\overline{h_2 u_2}^{1} h_3 \omega_3}^{2} - \overline{\overline{h_3 u_3}^{1} h_2 \omega_2}^{3}\right) - \nu \frac{h_1}{h}\left(\frac{\delta h_3 \omega_3}{\delta x_2} - \frac{\delta h_2 \omega_2}{\delta x_3}\right) - \frac{1}{h_1}\frac{\delta p}{\delta x_1}, \tag{13}$$

$$\frac{\partial u_2}{\partial t} = \frac{h_2}{h}\left(\overline{\overline{h_3 u_3}^{2} h_1 \omega_1}^{3} - \overline{\overline{h_1 u_1}^{2} h_3 \omega_3}^{1}\right) - \nu \frac{h_2}{h}\left(\frac{\delta h_1 \omega_1}{\delta x_3} - \frac{\delta h_3 \omega_3}{\delta x_1}\right) - \frac{1}{h_2}\frac{\delta p}{\delta x_2}, \tag{14}$$

$$\frac{\partial u_3}{\partial t} = \frac{h_3}{h}\left(\overline{\overline{h_1 u_1}^{3} h_2 \omega_2}^{1} - \overline{\overline{h_2 u_2}^{3} h_1 \omega_1}^{2}\right) - \nu \frac{h_3}{h}\left(\frac{\delta h_2 \omega_2}{\delta x_1} - \frac{\delta h_1 \omega_1}{\delta x_2}\right) - \frac{1}{h_3}\frac{\delta p}{\delta x_3}. \tag{15}$$

The discretized continuity and vorticity equations follow from (8) and (9) after replacing the partial derivatives by the finite differences:

$$\frac{1}{h}\left[\frac{\delta}{\delta x_1}\left(\frac{h u_1}{h_1}\right) + \frac{\delta}{\delta x_2}\left(\frac{h u_2}{h_2}\right) + \frac{\delta}{\delta x_3}\left(\frac{h u_3}{h_3}\right)\right] = 0, \tag{16}$$

$$\begin{aligned}
\omega_1 &= \frac{h_1}{h}\left(\frac{\delta h_3 u_3}{\delta x_2} - \frac{\delta h_2 u_2}{\delta x_3}\right),\\
\omega_2 &= \frac{h_2}{h}\left(\frac{\delta h_1 u_1}{\delta x_3} - \frac{\delta h_3 u_3}{\delta x_1}\right),\\
\omega_3 &= \frac{h_3}{h}\left(\frac{\delta h_2 u_2}{\delta x_1} - \frac{\delta h_1 u_1}{\delta x_2}\right).
\end{aligned} \tag{17}$$

To calculate the vorticity components down to the boundary points, the boundary conditions should be taken into account. Only normal-to-wall velocity components are defined directly at the boundaries, therefore the different expressions for the normal and tangential boundary conditions are used. Namely, at the surfaces, bounding the flow domain in the kth direction, i.e., for $x_k = x_k^{\mathrm{s}}, x_k^{\mathrm{e}}$ $(k = 1, 2, 3)$, the boundary conditions read

$$u_k = u_{\mathrm{b}k}, \quad h_m^{-1}\overline{h_m u_m}^k = u_{\mathrm{b}m}, \quad m \neq k. \tag{18}$$

Here, $u_{\mathrm{b}k}$ and $u_{\mathrm{b}m}$ stand for the ks and ms components of the boundary velocity $\mathbf{u}_{\mathrm{b}}$.

Similarly to the differential equations, the discretized equations obey several features. Let us denote by Grad, Div, and Curl the finite-difference analogues of the gradient, divergence, and curl operators, respectively. Note, first of all, that for any vector field $\mathbf{a}$ and any scalar field ϕ the identities are held

$$\mathrm{Div}\,\mathrm{Curl}\,\mathbf{a} \equiv 0, \quad \mathrm{Curl}\,\mathrm{Grad}\,\phi \equiv 0, \tag{19}$$

which are the analogues of the known differential identities. This in particular means, that vorticity field is a divergence-free irrespective of velocity field. Also, the discretized viscous terms of the NSE are divergence-free, which means that these terms are mass conserving. The consequence of the second identity (19) is that the pressure-gradient terms do not contribute to vorticity evolution directly.

Accurate description of the total kinetic energy balance is essential in turbulence simulations. The energy balance equation is derived by dot multiplication of $\mathbf{u}$ and (1) and integration over the flow domain. Suppose that the boundary velocity is zero, then the result will be the following:

$$\frac{\mathrm{d}E}{\mathrm{d}t} = -\nu \int_D |\boldsymbol{\omega}|^2 \,\mathrm{d}\mathbf{x}, \quad E = \frac{1}{2}\int_D |\mathbf{u}|^2 \,\mathrm{d}\mathbf{x}. \tag{20}$$

It is important that for a zero normal-to-wall boundary velocity (impermeability condition) the nonlinear and pressure-gradient terms of the NSE do not produce kinetic energy, but only redistribute it among the flow regions. The consequence of the no-slip boundary conditions with zero tangential velocity (steady boundaries) is a negativeness of the viscous term contribution.

In the discrete case kinetic energy is defined as

$$E = \frac{1}{2}\sum (\overline{u_1^2 h}^1 + \overline{u_2^2 h}^2 + \overline{u_3^2 h}^3) \Delta_1 \Delta_2 \Delta_3 \tag{21}$$

with summation over all pressure-nodes. The energy balance equation is derived from (21) by differentiation with respect to t and $\partial u_k/\partial t$ taken from (13)–(15). It is easy to show, that for divergence-free velocity field with zero normal-to-wall boundary velocities contribution of the pressure-gradient terms to the total kinetic energy production is identically zero. As regards the nonlinear terms, their contribution includes three pairs corresponding to the three vorticity components. Each pair produces a zero contribution. For example, contributions of the first term in (13) and of the second term in (14) are (the $\Delta_1\Delta_2\Delta_3$ multiplier is omitted)

$$\sum \overline{h u_1 \frac{h_1}{h} \overline{\overline{u_2 h_2}^1 \omega_3 h_3}^{21}}, \quad \sum \overline{h u_2 \frac{h_2}{h} \overline{\overline{u_1 h_1}^2 \omega_3 h_3}^{12}}.$$

For impermeable boundaries it is easy to see that both these expressions are equal to

$$\sum \overline{u_1 h_1}^2 \overline{u_2 h_2}^1 \omega_3 h_3$$

(with summation over ω_3-nodes) and thus, they vanish each other.

The nonlinear terms may be discretized in a different way. For example, the first term in (13) and the second term in (14) may be replaced with

$$\frac{1}{h}\overline{u_2}^1 \overline{\omega_3 h}^2 \quad \text{and} \quad \frac{1}{h}\overline{u_1}^2 \overline{\omega_3 h}^1 \tag{22}$$

also with zero contribution to the total energy production. The nonlinear terms in the discrete equations may be taken either in the form of (13)–(15), or in the form (22). Moreover, one pair of the nonlinear terms may be taken in one form, while the other two in another. This option will be exploited for the singularity elimination in polar coordinates.

It may be shown after simple algebraic manipulations that contribution of the viscous terms into the discrete energy equation is

$$-\nu \sum (\overline{\omega_1^2}^{h^{2,3}} + \overline{\omega_2^2}^{h^{1,3}} + \overline{\omega_3^2}^{h^{1,2}}) \Delta_1 \Delta_2 \Delta_3,$$

which is an approximation to the viscous dissipation expression in (20).

3.2. Pressure equation

Let us denote the right-hand-side terms of (13)–(15) except the pressure-gradient terms by $\mathbf{v} = (v_1, v_2, v_3)$. Then, the equations in vector form become

$$\frac{\partial \mathbf{u}}{\partial t} = \mathbf{v} - \operatorname{Grad} p. \tag{23}$$

Pressure equation is a consequence of the divergenceless of $\partial \mathbf{u}/\partial t$

$$\operatorname{Div} \operatorname{Grad} p = \operatorname{Div} \mathbf{v}. \tag{24}$$

Pressure boundary conditions follow from (23) and the boundary conditions for the normal velocity components

$$\left. \frac{\partial \mathbf{u}}{\partial t} \cdot \mathbf{n} \right|_\Gamma = \left. \frac{\partial \mathbf{u}_\mathrm{b}}{\partial t} \cdot \mathbf{n} \right|_\Gamma,$$

which leads to[1]

$$\frac{1}{h_k} \frac{\delta p}{\delta x_k} = v_k - \frac{\partial u_{\mathrm{b}k}}{\partial t}, \quad x_k = x_k^\mathrm{s}, x_k^\mathrm{e}, \qquad k = 1, 2, 3. \tag{25}$$

It is essential that only the normal (and not tangential) component of the velocity boundary conditions is needed to find the pressure. This is because only the normal-to-boundary velocity component may affect the amount of fluid inside the flow domain and, thus, the incompressibility. From the physical considerations, the divergenceless of $\partial \mathbf{u}/\partial t$ is possible only for a zero boundary flux

$$\sum \frac{\partial \mathbf{u}_\mathrm{b}}{\partial t} \cdot \mathbf{n} \Delta_S = 0. \tag{26}$$

Here, summation is extended over all boundary cell faces; Δ_S is a surface element, at the boundary normal to kth direction $\Delta_S = h\Delta_1\Delta_2\Delta_3/(h_k\Delta_k)$. It is easy to show that (26) is a solvability condition for the problem (24) and (25) as well as for the variant mentioned in the footnote.

3.3. Time advancement

The spatial discretization of the incompressible NSE with sufficiently fine resolution leads to stiff problems and requires implicit methods for time advancement. Semi-implicit methods, where only a part of the Navier–Stokes operator is treated implicitly, are most efficient for turbulent flow simulations. We assume, that the implicit terms are linear and denote them as $L\mathbf{u}$. The corresponding operator L will be referred as *implicit operator*. We propose the following 3-step procedure [35] to advance from the velocity field $\mathbf{u} = \mathbf{u}^m$ at the time moment $t = t^m$ to $\mathbf{u} = \mathbf{u}^{m+1}$ at the moment $t = t^{m+1} = t^m + \Delta t$.

Step 1: $\mathbf{v}^m = \mathbf{u}^m \times \boldsymbol{\omega}^m - \nu \operatorname{Curl} \boldsymbol{\omega}^m, \mathbf{w}^m = \mathbf{v}_m - \operatorname{Grad} p^m$, $\operatorname{Div} \mathbf{w}^m = 0$, $\mathbf{w}^m \cdot \mathbf{n}|_\Gamma = \frac{\partial \mathbf{u}_\mathrm{b}(t^m)}{\partial t} \cdot \mathbf{n}$;

$$\frac{\mathbf{u}' - \mathbf{u}^m}{\Delta t} = \frac{2}{3}\mathbf{w}^m + \frac{1}{3} L(\mathbf{u}' - \mathbf{u}^m). \tag{27}$$

[1] A more practicable and algebraically identical way is to set $v_k = \partial u_{\mathrm{b}k}/\partial t$ at the boundaries and to solve (24) with zero boundary conditions $h_k^{-1}\delta p/\delta x_k = 0$.

Step 2: $\mathbf{v}' = \mathbf{u}' \times \boldsymbol{\omega}' - \nu \operatorname{Curl} \boldsymbol{\omega}', \mathbf{w}' = \mathbf{v}' - \operatorname{Grad} p', \operatorname{Div} \mathbf{w}' = 0, \ \mathbf{w}' \cdot \mathbf{n}|_\Gamma = \frac{\partial \mathbf{u}_b(t^m + 2\Delta t/3)}{\partial t} \cdot \mathbf{n};$

$$\frac{\mathbf{u}'' - \mathbf{u}^m}{\Delta t} = \frac{1}{3}\mathbf{w}^m + \frac{1}{3}\mathbf{w}' + \frac{1}{3}L(\mathbf{u}'' - \mathbf{u}'). \tag{28}$$

Step 3: $\bar{\mathbf{u}} = (9\mathbf{u}' - 3\mathbf{u}'' - 2\mathbf{u}^m)/4,$

$$\frac{\tilde{\mathbf{u}} - \mathbf{u}^m}{\Delta t} = \frac{1}{4}\mathbf{w}^m + \frac{3}{4}\mathbf{w}' + \frac{1}{3}L(\tilde{\mathbf{u}} - \bar{\mathbf{u}}). \tag{29}$$

$\mathbf{v}'' = \mathbf{u}'' \times \boldsymbol{\omega}'' - \nu \operatorname{Curl} \boldsymbol{\omega}'',$

$$\frac{\hat{\mathbf{u}} - \mathbf{u}^m}{\Delta t} = \frac{1}{4}\mathbf{w}^m + \frac{3}{4}(\mathbf{v}'' - \operatorname{Grad} p') + \frac{1}{3}L(\hat{\mathbf{u}} - \tilde{\mathbf{u}}); \tag{30}$$

$\mathbf{u}^{m+1} = \hat{\mathbf{u}} - \operatorname{Grad} q, \ \operatorname{Div} \mathbf{u}^{m+1} = 0, \ \mathbf{u}^{m+1} \cdot \mathbf{n}|_\Gamma = \mathbf{u}_b(t^{m+1}) \cdot \mathbf{n}.$

The first and the second steps of the scheme consist of the three successive substeps: (i) calculation of the vorticity, nonlinear and viscous terms of the NSE, (ii) projection to the space of divergenceless vectors and calculation of the pressure according to the procedure of the previous section, (iii) solution of the linear set of equations connected with the implicit operator. The third step includes one more substep (iii) and besides that, the pressure substep is performed last to ensure the divergenceless of the final velocity field. The scheme possesses overall third-order accuracy unlike the other 3-step Runge–Kutta based semi-implicit schemes [9,22,33,34] which are second-order accurate.[2]

The availability of two approximations to the final velocity

$$\mathbf{u}^{m+1} = \mathbf{u}(t^{m+1}) + \mathrm{O}(\Delta t^4) \quad \text{and} \quad \tilde{\mathbf{u}} = \mathbf{u}(t^{m+1}) + \mathrm{O}(\Delta t^3)$$

enables to estimate the local accuracy of time integration and to control the time-step size. The corresponding algorithms are given in [21,35].

It is important that no specific boundary conditions are needed when solving equations including L operator. Eqs. (27)–(30) should be solved only for internal grid points, while in the boundary points velocities (normal to boundary) are obtained from the boundary conditions. Each of (27)–(30) is reduced to the form

$$(I - \tau L)\mathbf{x} = \mathbf{y}, \quad \tau = \frac{1}{3}\Delta t, \tag{31}$$

where I is the identity operator, and $\mathbf{x}$ is the argument of L in the right-hand side of (27)–(30). For example, for (30) $\mathbf{x} = \hat{\mathbf{u}} - \tilde{\mathbf{u}}$ and $\mathbf{y} = \Delta t[0.25\mathbf{w}^m + 0.75(\mathbf{v}'' - \operatorname{Grad} p')] - (\tilde{\mathbf{u}} - \mathbf{u}^m)$. Eq. (31) is solved with zero boundary conditions for $\mathbf{x}$ even in the case of unsteady velocity boundary conditions.

3.4. Choice of implicit operator

Specific form of the implicit operator does not affect formal order of accuracy of the scheme, but determines its stability properties. In the trivial case of $L \equiv 0$ the scheme turns into a simple third-order accurate explicit Runge–Kutta scheme. Generally speaking, the stability is the higher, the closer L is to the Jacobian of the Navier–Stokes operator. An important criterion for choosing L is how effectively may be solved the corresponding set of linear Eq. (31). In simulations of wall-bounded flows L is usually taken as a factorized viscous term operator of the NSE. Let us decompose the viscous term of the NSE to a sum of three terms $(L_1 + L_2 + L_3)\mathbf{u}$, then L is defined from the expression

$$(I - \tau L) = (I - \tau L_1)(I - \tau L_2)(I - \tau L_3). \tag{32}$$

Thus, solution of (31) is reduced to the successive solution of three systems. If the matrices L_k have simple structure then the entire problem can be solved effectively. In Cartesian coordinates a second derivative in kth spatial direction is often taken as L_k. Then solution of (31) reduces to the successive solution of tridiagonal systems.

[2] Numerical evidence of the third-order accuracy of the present scheme is given in Appendix A.

In curvilinear orthogonal coordinates the following way for the viscous term decomposition can be proposed. It based on the representation of the divergence and curl operators as

$$\mathrm{Div}\,\mathbf{u} = \frac{1}{h}\sum_{k=1}^{3}\frac{\delta}{\delta x_k}\frac{hu_k}{h_k}, \quad \mathrm{Curl}\,\boldsymbol{\omega} = \begin{vmatrix} \frac{h_1}{h}\mathbf{j}_1 & \frac{h_2}{h}\mathbf{j}_2 & \frac{h_3}{h}\mathbf{j}_3 \\ \frac{\delta}{\delta x_1} & \frac{\delta}{\delta x_2} & \frac{\delta}{\delta x_3} \\ h_1\omega_1 & h_2\omega_2 & h_3\omega_3 \end{vmatrix}.$$

The viscous term in general case then can be written as

$$\nu(\mathrm{Grad}\,\mathrm{Div}\,\mathbf{u} - \mathrm{Curl}\,\boldsymbol{\omega}) = (L_1 + L_2 + L_3)\mathbf{u},$$

where

$$L_1\mathbf{u} = \nu\left(\mathrm{Grad}\,\frac{1}{h}\frac{\delta}{\delta x_1}\frac{hu_1}{h_1} - \begin{vmatrix} \frac{h_1}{h}\mathbf{j}_1 & \frac{h_2}{h}\mathbf{j}_2 & \frac{h_3}{h}\mathbf{j}_3 \\ \frac{\delta}{\delta x_1} & 0 & 0 \\ h_1\omega_1 & h_2\omega_2 & h_3\omega_3 \end{vmatrix}\right)$$

$$\equiv \nu\begin{pmatrix} \frac{1}{h_1}\frac{\delta}{\delta x_1}\frac{1}{h}\frac{\delta}{\delta x_1}\frac{hu_1}{h_1} \\ \frac{h_2}{h}\frac{\delta}{\delta x_1}\frac{h_3^2}{h}\frac{\delta h_2 u_2}{\delta x_1} + \left(\frac{1}{h_2}\frac{\delta}{\delta x_2}\frac{1}{h}\frac{\delta}{\delta x_1}\frac{hu_1}{h_1} - \frac{h_2}{h}\frac{\delta}{\delta x_1}\frac{h_3^2}{h}\frac{\delta h_1 u_1}{\delta x_2}\right) \\ \frac{h_3}{h}\frac{\delta}{\delta x_1}\frac{h_2^2}{h}\frac{\delta h_3 u_3}{\delta x_1} + \left(\frac{1}{h_3}\frac{\delta}{\delta x_3}\frac{1}{h}\frac{\delta}{\delta x_1}\frac{hu_1}{h_1} - \frac{h_3}{h}\frac{\delta}{\delta x_1}\frac{h_2^2}{h}\frac{\delta h_1 u_1}{\delta x_3}\right) \end{pmatrix}, \tag{33}$$

$$L_2\mathbf{u} = \nu\left(\mathrm{Grad}\,\frac{1}{h}\frac{\delta}{\delta x_2}\frac{hu_2}{h_2} - \begin{vmatrix} \frac{h_1}{h}\mathbf{j}_1 & \frac{h_2}{h}\mathbf{j}_2 & \frac{h_3}{h}\mathbf{j}_3 \\ 0 & \frac{\delta}{\delta x_2} & 0 \\ h_1\omega_1 & h_2\omega_2 & h_3\omega_3 \end{vmatrix}\right)$$

$$\equiv \nu\begin{pmatrix} \frac{h_1}{h}\frac{\delta}{\delta x_2}\frac{h_3^2}{h}\frac{\delta h_1 u_1}{\delta x_2} + \left(\frac{1}{h_1}\frac{\delta}{\delta x_1}\frac{1}{h}\frac{\delta}{\delta x_2}\frac{hu_2}{h_2} - \frac{h_1}{h}\frac{\delta}{\delta x_2}\frac{h_3^2}{h}\frac{\delta h_2 u_2}{\delta x_1}\right) \\ \frac{1}{h_2}\frac{\delta}{\delta x_2}\frac{1}{h}\frac{\delta}{\delta x_2}\frac{hu_2}{h_2} \\ \frac{h_3}{h}\frac{\delta}{\delta x_2}\frac{h_1^2}{h}\frac{\delta h_3 u_3}{\delta x_2} + \left(\frac{1}{h_3}\frac{\delta}{\delta x_3}\frac{1}{h}\frac{\delta}{\delta x_2}\frac{hu_2}{h_2} - \frac{h_3}{h}\frac{\delta}{\delta x_2}\frac{h_1^2}{h}\frac{\delta h_2 u_2}{\delta x_3}\right) \end{pmatrix}, \tag{34}$$

$$L_3\mathbf{u} = \nu\left(\mathrm{Grad}\,\frac{1}{h}\frac{\delta}{\delta x_3}\frac{hu_3}{h_3} - \begin{vmatrix} \frac{h_1}{h}\mathbf{j}_1 & \frac{h_2}{h}\mathbf{j}_2 & \frac{h_3}{h}\mathbf{j}_3 \\ 0 & 0 & \frac{\delta}{\delta x_3} \\ h_1\omega_1 & h_2\omega_2 & h_3\omega_3 \end{vmatrix}\right)$$

$$\equiv \nu\begin{pmatrix} \frac{h_1}{h}\frac{\delta}{\delta x_3}\frac{h_2^2}{h}\frac{\delta h_1 u_1}{\delta x_3} + \left(\frac{1}{h_1}\frac{\delta}{\delta x_1}\frac{1}{h}\frac{\delta}{\delta x_3}\frac{hu_3}{h_3} - \frac{h_1}{h}\frac{\delta}{\delta x_3}\frac{h_2^2}{h}\frac{\delta h_3 u_3}{\delta x_1}\right) \\ \frac{h_2}{h}\frac{\delta}{\delta x_3}\frac{h_1^2}{h}\frac{\delta h_2 u_2}{\delta x_3} + \left(\frac{1}{h_2}\frac{\delta}{\delta x_2}\frac{1}{h}\frac{\delta}{\delta x_3}\frac{hu_3}{h_3} - \frac{h_2}{h}\frac{\delta}{\delta x_3}\frac{h_1^2}{h}\frac{\delta h_3 u_3}{\delta x_2}\right) \\ \frac{1}{h_3}\frac{\delta}{\delta x_3}\frac{1}{h}\frac{\delta}{\delta x_3}\frac{hu_3}{h_3} \end{pmatrix}. \tag{35}$$

The characteristic feature of (33)–(35) operators is their generalized commutativity with a gradient operator

$$L_k\mathrm{Grad}\,\phi = \mathrm{Grad}\,M_k\phi, \quad M_k = \nu\frac{1}{h}\frac{\delta}{\delta x_k}\frac{h}{h_k^2}\frac{\delta}{\delta x_k}, \tag{36}$$

which leads to analogous feature of operator L, defined in (32).[3] It is easy to see that such a decomposition of the viscous term requires solution of only tridiagonal systems of equations when solving (31).

The author's experience suggests that in the case of a nonsingular coordinate system operators L_k may be simplified while keeping the acceptable stability of time advancement. In simulations of wall-bounded flows the minimal mesh size in the wall-normal direction is usually smaller than the mesh sizes in the other

[3] The commutativity rule (36) is violated in the points adjacent to the boundaries when L_k operators are considered with no-slip boundary conditions for the tangential velocities. However, the rule holds up to the boundaries for periodic and shear-free boundary conditions.

directions. If the mesh size in some direction does not restrict stability of time advancement then it is unreasonable to include the corresponding operators into L. This may reduce the time required for time integration. It should be noted, however, that the costs connected with the implicit operator resolution (when the approximate factorization technique is applied) is usually significantly less than, say, the costs connected with the pressure calculation. Therefore, the overall time savings of such simplifications are not considerable.

Other forms of the implicit operator may be used depending on the specific features of the computational mesh and the flow under consideration. In particular, some linearization of convective terms may be included into implicit operator to weaken numerical stability restrictions. Such a possibility will be considered below.

4. Numerical tests

In this section some applications of the method to different flows are presented. Comparison with numerical results obtained by different methods are also shown to prove the qualities of the method.

4.1. Cartesian coordinates. Turbulent channel flow at $Re_\tau = 180$

Since the classical work of Kim et al. [5], fully developed channel flow at $Re_\tau = 180$ is used intensively to test the accuracy and robustness of numerical techniques (see, for example [9,33,40,41]). Although the flow geometry implies the use of Cartesian rather than curvilinear coordinates, this test case is included into the paper because of untraditional spatial discretization involved in the present method.

The flow domain is a rectangular box in Cartesian coordinates of the size $L_x \times 2\delta \times L_z$ in the streamwise, wall-normal, and spanwise directions, respectively. Computational coordinates x_k and metric stretching factors h_k are defined from

$$x = x_1, \quad y = y(x_2), \quad z = x_3,$$
$$h_1 = 1, \quad h_2(x_2) = y'(x_2), \quad h_3 = 1.$$

Hyperbolic tangent function $y(x_2)$ is used to obtain the mesh nodes clustering in the vicinity of the rigid boundaries. The present simulations were carried out in the box with $L_x = 2\pi\delta$, $L_z = \pi\delta$ at Reynolds number 4200 based on the laminar centerline velocity U_l ($U_l = 1.5U_b$, where U_b is the bulk velocity which is kept fixed during the calculations) and the channel half-width δ. In a developed turbulent regime this corresponds to a Reynolds number Re_τ of about 180, based on the turbulent wall velocity u_τ, and the channel half-width.[4] The $128 \times 128 \times 128$ mesh was used with spacing $\Delta_x^+ \approx 8.8$ and $\Delta_z^+ \approx 4.4$ in the streamwise and spanwise directions. The spacing in the wall-normal direction varied from 0.65 to 5.1 wall units. Time-integration was performed with the time-steps $\Delta t = 0.025\delta/U_l \approx 0.2\nu/u_\tau^2$ and $\Delta t = 0.05\delta/U_l \approx 0.4\nu/u_\tau^2$. The negligible differences were detected in statistical results obtained with these two time-steps, while the results for the larger step $\Delta t = 0.1\delta/U_l$ reveal considerable deviations. This observation supports the hypothesis of [40] that $\Delta t^+ = 0.4$ is the largest time-step which accurately predicts turbulent statistics in turbulent channel flow at a given Reynolds number.[5]

The mean properties of the flow computed with the present scheme are in excellent agreement with the results of Kim et al. [5] obtained by a fully spectral method with $192 \times 129 \times 160$ grid points in computational box of a size $4\pi\delta \times 2\delta \times 2\pi\delta$. The skin friction coefficient, $C_f = \tau_w/\frac{1}{2}\rho U_b^2$ is 8.06×10^{-3}, which coincides with the value obtained in [5] to -1.5%. The mean centerline velocity U_c^+ is 18.32 ($+0.7\%$) and $U_c/U_b = 1.16$ just as in [5].

The profiles of the mean velocity, root-mean-square velocity fluctuations, Reynolds shear stress, and root-mean-square vorticity fluctuations in the near-wall region are shown in Fig. 2 and compared with the simulation results by Kim et al. [5] and by Horiuti [42]. The latter are obtained by a fully spectral method with $128 \times 128 \times 128$ grid points in computational box of a size $12.8\delta \times 2\delta \times 6.4\delta$. The dashed line in Fig. 2(a) represents the law of the wall and the log law with the same additive constant 5.5 as in [5]. The comparison of the

[4] Wall units of velocity $u_\tau = \sqrt{\tau_w/\rho}$ and length $l_\tau = \nu/u_\tau$ are defined using mean wall shear stress τ_w. Normalization by the wall units is denoted by a superscript $+$.

[5] This hypothesis was refuted in [41], where little variation in turbulent statistics was observed up to $\Delta t^+ = 1.6$ when using a fully conservative scheme.

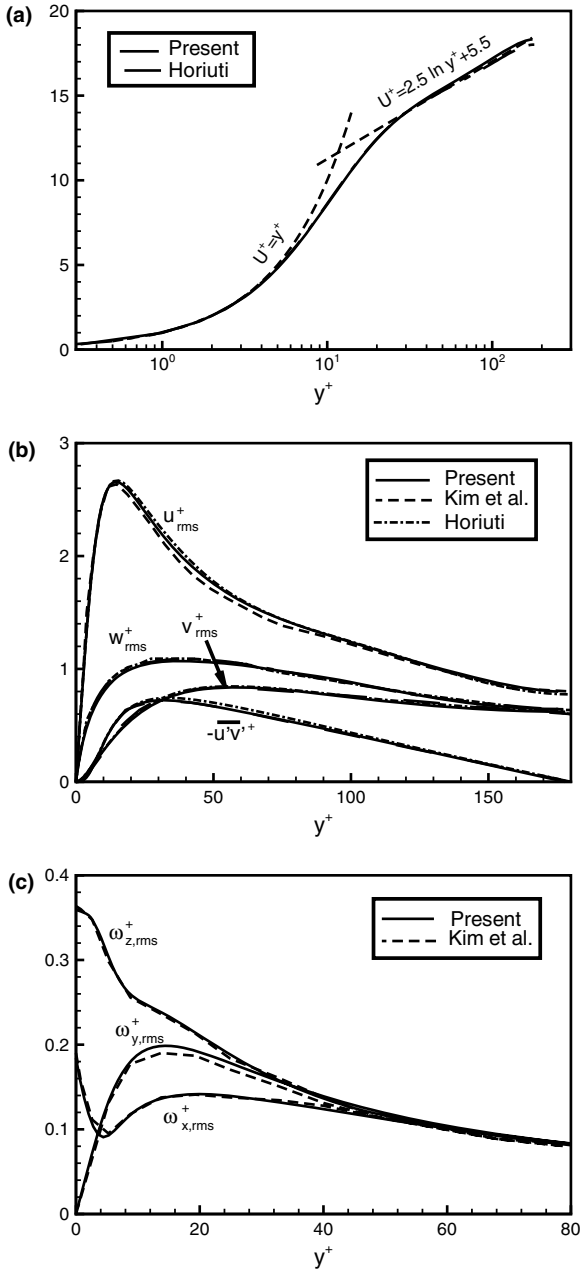

Fig. 2. Turbulent channel flow at $Re_\tau = 180$. (a) Mean velocity profile; (b) rms velocity fluctuations and Reynolds shear stress; (c) rms vorticity fluctuations. Present results are compared with DNS data of Kim et al. [5] and Horiuti [42].

present results with those, obtained by fully spectral methods, show excellent agreement and prove the reasonable accuracy of the method.

4.2. Cylindrical coordinates

An extensive literature is devoted to different aspects of numerical solution of the NSE in cylindrical polar coordinates: [7,19,21–28]. Of particular interest are the conservation properties of numerical schemes and treatment of coordinate singularities. Both these problems have relatively simple solutions within a present method.

Consider for definiteness a pipe flow geometry. Computational coordinates $(x_1, x_2, x_3) = (\rho, \theta, z)$ are cylindrical coordinates stretched in the radial direction to get a grid node clustering near the rigid boundary

$$x = r\cos\theta, \quad y = r\sin\theta, \quad r = r(\rho).$$

The metric stretching factors $(h_1, h_2, h_3) = (h_\rho, h_\theta, h_z)$ have the following values:

$$h_\rho(\rho) = r', \quad h_\theta(\rho) = r, \quad h_z = 1.$$

According to Eqs. (13)–(17) the discretized NSE, continuity, and vorticity equations have the following form:

$$\frac{\partial u_\rho}{\partial t} = \overline{\overline{u_\theta}^{\rho}\omega_z}^{\theta} - \overline{\overline{u_z}^{\rho}\omega_\theta}^{z} - \nu\left(\frac{1}{r}\frac{\delta\omega_z}{\delta\theta} - \frac{\delta\omega_\theta}{\delta z}\right) - \frac{1}{r'}\frac{\delta p}{\delta\rho}, \tag{37}$$

$$\frac{\partial u_\theta}{\partial t} = \overline{\overline{u_z}^{\theta}\omega_\rho}^{z} - \frac{1}{rr'}\overline{\overline{u_\rho}^{\theta} r r' \omega_z}^{\rho} - \nu\left(\frac{\delta\omega_\rho}{\delta z} - \frac{1}{r'}\frac{\delta\omega_z}{\delta\rho}\right) - \frac{1}{r}\frac{\delta p}{\delta\theta}, \tag{38}$$

$$\frac{\partial u_z}{\partial t} = \frac{1}{rr'}\overline{\overline{u_\rho}^{z} r r' \omega_\theta}^{\rho} - \overline{\overline{u_\theta}^{z}\omega_\rho}^{\theta} - \nu\left(\frac{1}{rr'}\frac{\delta r\omega_\theta}{\delta\rho} - \frac{1}{r}\frac{\delta\omega_\rho}{\delta\theta}\right) - \frac{\delta p}{\delta z}, \tag{39}$$

$$\frac{1}{rr'}\frac{\delta r u_\rho}{\delta\rho} + \frac{1}{r}\frac{\delta u_\theta}{\delta\theta} + \frac{\delta u_z}{\delta z} = 0, \tag{40}$$

$$\omega_\rho = \frac{1}{r}\frac{\delta u_z}{\delta\theta} - \frac{\delta u_\theta}{\delta z}, \quad \omega_\theta = \frac{\delta u_\rho}{\delta z} - \frac{1}{r'}\frac{\delta u_z}{\delta\rho}, \quad \omega_z = \frac{1}{rr'}\frac{\delta r u_\theta}{\delta\rho} - \frac{1}{r}\frac{\delta u_\rho}{\delta\theta}. \tag{41}$$

The pair of nonlinear terms in the NSE containing ω_z, i.e., the first term in (37) and the second term in (38), are written in the form of (22), while the other two pairs are written in the regular form of (13)–(15). This is done in order to eliminate a need of u_ρ determination at the pole axis (i.e., at $r = 0$). In the regular form the second nonlinear term in (38) would read $\frac{1}{r'}\overline{\overline{u_\rho}^{\theta} r' \omega_z}^{\rho}$. Thus, to evaluate $\partial u_\theta/\partial t$ in the nearest to the pole points one would had to know the value of u_ρ at $r = 0$. Everywhere in (38)–(40) u_ρ appears in the combination ru_ρ which may be set to zero at $r = 0$, thus, the value of u_ρ at $r = 0$ is not needed, and (37) may be solved only for grid points with $r > 0$. Similarly, the vorticity component ω_θ at $r = 0$ in (39) appears as $r\omega_\theta$ and, thus, does not need to be determined.

The only quantity needed to be found at the pole is the axial vorticity ω_z. For its evaluation the Stokes theorem may be used, according to which the velocity circulation along a closed contour is equal to the vorticity flux through a surface bounded by the contour. For each z consider the normal to the pole axis circular contour, connecting the nearest to the pole grid points: $\rho = \Delta_\rho/2$, $\theta = \theta_n$. The radius of this contour is $r_c = r(\Delta_\rho/2)$. The velocity circulation Γ and the vorticity flux Π for this contour to the second order of accuracy are equal to

$$\Gamma = \sum_{n=1}^{N_\theta} u_\theta(\Delta_\rho/2, \theta_n, z)\Delta_\theta r_c, \quad \Pi = \omega_z(r = 0, z)\pi r_c^2.$$

Here, Δ_ρ and $\Delta_\theta = 2\pi/N_\theta$ are the grid spacings in the ρ and θ coordinates, N_θ is the number of grid points in θ direction, and $\theta_n = n\Delta_\theta$. The expression for the axial vorticity at the pole follows from equating Γ and Π

$$\omega_z(r = 0, z) = \frac{2}{r_c}\frac{1}{N_\theta}\sum_{n=1}^{N_\theta} u_\theta(\Delta_\rho/2, \theta_n, z), \quad r_c = r(\Delta_\rho/2). \tag{42}$$

Note, that the described method of radial coordinate treatment including the pole condition for the axial vorticity was first proposed in [21], within a mixed spectral/finite-difference method and was thoroughly tested in [8,9].

The pole condition (42) is used for the evaluation $\delta\omega_z/\delta\rho$ $(=\delta\omega_3/\delta x_1)$ in (38) as well as in the implicit operator L_1 (33).

4.2.1. Turbulent pipe flow at $Re_\tau = 180$

Turbulent pipe flow at $Re_\tau = 180$ has been studied numerically in details in previous papers [7,23,27]. DNS for the close Reynolds number $Re_\tau = 200$ has been carried out in [9]. In the present paper, calculations were performed with the aim to compare results with those of Unger and Friedrich [7] and Fukagata and Kasagi

[27] which are available in tabulated forms at the website (http://www.thtlab.t.u-tokio.ac.jp/).[6] In all simulations the length of computational domain was $10R$ (R is the pipe radius), and the spatial resolution was $96 \times 128 \times 256$ in the radial, azimuthal, and axial directions, respectively.

A polynomial radial coordinate stretching $r(\rho)$ was used in the present simulations, producing the grid spacing $\Delta_r \approx r' \Delta_\rho$ in the range from 0.47 wall units near the wall to 3.1 wall units near the centerline. The results of all three DNS are presented in Fig. 3 demonstrating an excellent agreement in the mean velocity, rms velocity fluctuations, and Reynolds shear stress profiles. The profiles of rms vorticity fluctuations obtained by the present method are almost identical with those of [27], while the results of Unger and Friedrich reveal some deviations in the near-wall region (in $\omega_{\theta,\mathrm{rms}}$ profile) and considerable deviations in the core of the flow, especially near the pipe's axis of symmetry (in $\omega_{z,\mathrm{rms}}$ and $\omega_{\theta,\mathrm{rms}}$ profiles). The latter effect may be attributed to either weak instability of time integration or inadequate pole treatment in the method of [7].

In [7] the equally spaced grid in the r-direction was used with $\Delta_r^+ = 1.88$. Only the terms with derivatives in the azimuthal direction were treated implicitly in the time-stepping procedure, so numerical stability considerations limited the maximum time-step to $\Delta t = 0.0004R/u_\tau \approx 0.072\nu/u_\tau^2$. Akselvoll and Moin [23] suggested to treat implicitly different terms in different flow regions and were able to increase the time-step up to $\Delta t = 0.001R/u_\tau$ within the 3-step Runge–Kutta/Crank–Nicolson scheme of [33]. The same time-step was used in [27]. The present simulations were performed with $\Delta t = 0.05R/U_1 \approx 0.3\nu/u_\tau^2$ (U_1 is the laminar centerline velocity) which is 4 times larger than that used in [7] and $\frac{5}{3}$ times larger than that used in [23,27]. Note that only viscous and no convective terms were treated implicitly.

4.2.2. Lamb dipole

Calculation of a Lamb dipole flow in cylindrical coordinates was suggested in [22] as a test case of a flow crossing the polar axis. This flow is not a good application for polar coordinates but presents a severe test for code accuracy and stability. The vorticity distribution for a Lamb dipole is

$$\omega_z(\hat{\rho}, \phi) = \frac{2kU}{J_0(ka)} J_1(k\hat{\rho}) \sin\phi, \quad 0 \leqslant \hat{\rho} \leqslant a, \tag{43}$$

where $\hat{\rho}$ and ϕ are, respectively, radial and azimuthal coordinates of a polar frame of reference with the origin in the center of the dipole. When $ka = 3.83$ the inviscid dipole is moved with a self-induced translation velocity equal to U.

The present calculations were performed at Reynolds number $Re = Ua/\nu = 1000$ in a circular computational domain of a radius $2.5a$ with the shear-free boundary conditions and spatial resolution 96×128 in the radial and azimuthal directions. Dipole velocity U and dipole radius a are taken as the velocity and length scales. The vorticity map corresponding to (43) is shown in Fig. 4(a) for a dipole centered off-axis. In the successive Fig. 4(b) and (c) is displayed the motion of the structure towards the right due to the self-induced translation velocity, until the vortex has completely passed through the origin, without observing any distortion of the vortex due to the discretization.

As was noted in [22] calculations of the Lamb dipole in cylindrical coordinates requires very small time-step, since the cells become very small near the origin and velocities are high. However, the concrete values of the time-step were not given in [22]. It is a convenient case to demonstrate how the choice of implicit operator in the time-advancing procedure affect the efficiency of the method. For the explicit method ($L \equiv 0$), the most severe restriction on the time-step size follows from the large negative eigenvalues of the viscous-term operator. For the third-order accurate Runge–Kutta scheme it reads $\Delta t \lesssim 2.5/|\Lambda|$, where Λ is the eigenvalue with the largest modulus. For the case under consideration, it may be estimated as $\Lambda \approx -1/(\Delta_{\min}^2 Re)$ with $\Delta_{\min}$ as a minimal grid spacing in the mesh. For the given mesh and flow parameters, $\Delta_{\min} = 0.5\Delta_r\Delta_\theta \approx 6.4 \times 10^{-4}$ which leads to $\Delta t \approx 1.02 \times 10^{-3}$ as a stability limit. This estimate conforms with the explicit calculations.

The removal of the 'viscous' instability by means of using L in the form of (32)–(35) extends the range of stable integration up to $\Delta t = 5.0 \times 10^{-3}$. Fig. 4 corresponds to $\Delta t = 4.0 \times 10^{-3}$ with this kind of the implicit

[6] Another DNS presented in [7] was performed by Eggels and Nieuwstadt using a similar code as Unger and Friedrich. Only results of Unger and Friedrich are used for comparison in the present paper because their data for rms vorticity fluctuations are available at the website.

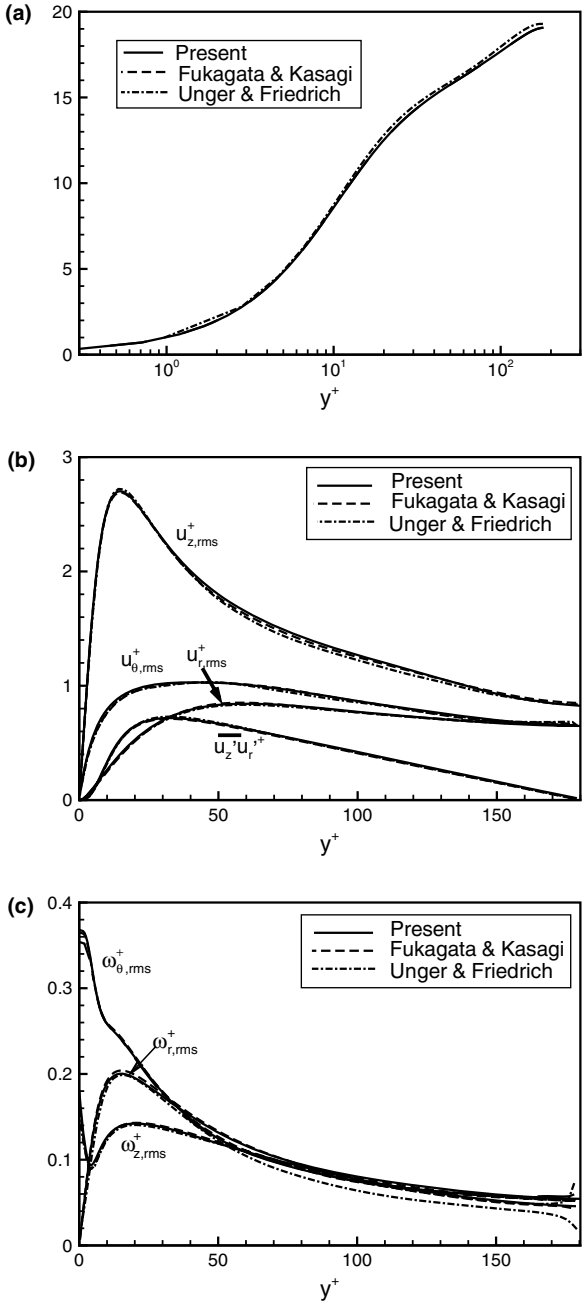

Fig. 3. Turbulent pipe flow at $Re_\tau = 180$. (a) Mean velocity profile; (b) rms velocity fluctuations and Reynolds shear stress; (c) rms vorticity fluctuations. Present results are compared with DNS data of Fukagata and Kasagi [27] and Unger and Friedrich [7].

operator. Note, that for $\Delta t = 5.0 \times 10^{-3}$ the maximal CFL number attains a value as high as CFL = 8, however, the instability does not arise because of the compensative viscous damping.

Stability of the time advancing may be further increased if the main contribution of linearized convective term is included into the implicit operator. The L in the factorized form $(I - \tau L) = (I - \tau \hat{L}_1)(I - \tau \hat{L}_2)$ with

$$\hat{L}_1 \mathbf{u} = L_1 \mathbf{u} - \begin{pmatrix} \frac{1}{r} u_\rho^m \left(\frac{1}{r'} \frac{\delta \overline{r u_\rho}^\rho}{\delta \rho} - u_\rho \right) \\ \frac{1}{r r'} \overline{r u_\rho^m}^{\rho,\theta} \frac{\delta \overline{u_\theta}^\rho}{\delta \rho} \end{pmatrix}, \quad \hat{L}_2 \mathbf{u} = L_2 \mathbf{u} - \begin{pmatrix} \frac{1}{r} \overline{u_\theta^m}^{\rho,\theta} \frac{\delta \overline{u_\rho}^\theta}{\delta \theta} \\ \frac{1}{r} u_\theta^m \frac{\delta \overline{u_\theta}^\theta}{\delta \theta} \end{pmatrix} \tag{44}$$

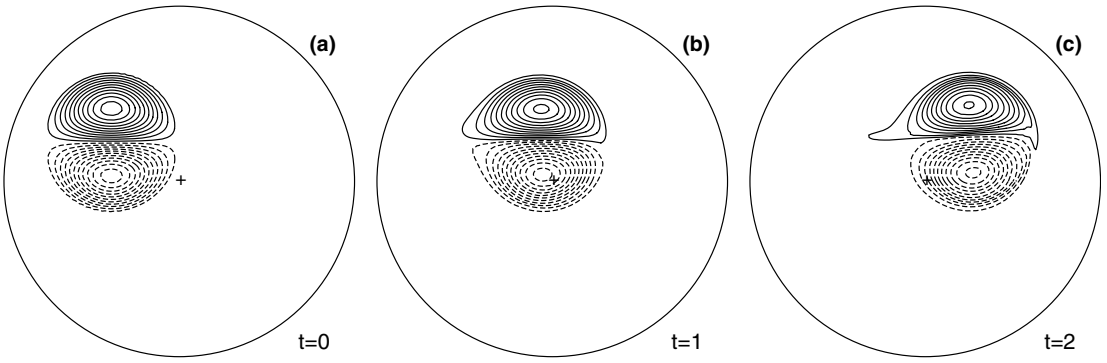

Fig. 4. Vorticity maps of the Lamb dipole at $t = 0$, $t = 1$ and $t = 2$.

moves the stability bound to $\Delta t = 3.3 \times 10^{-2}$. In (44) L_1 and L_2 operators are the 2D reduction of (33) and (34).

4.3. Cylindrical elliptic coordinates

Cylindrical elliptic coordinates (ξ, η, z) are defined as follows:

$$x = c\cosh\xi\cos\eta, \quad y = c\sinh\xi\sin\eta, \quad z = z.$$

In a plane, normal to z-direction, coordinate lines constitute a set of confocal hyperbolas ($\eta =$ constant – lines) and a set of confocal ellipses ($\xi =$ constant – lines). The focuses are located in the points $(x, y) = (-c, 0)$ and $(c, 0)$. It may be useful to provide a mesh stretching both in the ξ and η directions, then the computational coordinates (x_1, x_2, x_3) and the corresponding metric stretching factors (h_1, h_2, h_3) are defined from the following:

$$\xi = \xi(x_1), \quad \eta = \eta(x_2), \quad z = x_3,$$
$$h_1(x_1, x_2) = h_0\xi', \quad h_2(x_1, x_2) = h_0\eta', \quad h_3 = 1,$$
$$h_0(x_1, x_2) = c\sqrt{\sinh^2\xi + \sin^2\eta}.$$

The discrete equations follow directly from (13)–(17). The only singularities in the equations exist in the focuses points where the values of ω_3 must be defined. A simple and stable way is to get ω_3 in the focus for each x_3 from the expression for Cartesian coordinates $\omega_3 = \delta u_y/\delta x - \delta u_x/\delta y$, where $\delta u_y/\delta x$ and $\delta u_x/\delta y$ are evaluated with a second order of accuracy using u_1,u_2 in the nearest grid nodes.

In elliptic coordinates, the discrete Laplace operator, Div Grad, has the following form:

$$\frac{1}{h_0^2}\left(\frac{1}{\xi'}\frac{\delta}{\delta x_1}\frac{1}{\xi'}\frac{\delta}{\delta x_1} + \frac{1}{\eta'}\frac{\delta}{\delta x_2}\frac{1}{\eta'}\frac{\delta}{\delta x_2}\right) + \frac{\delta^2}{\delta x_3^2}. \tag{45}$$

In the general case solution of the pressure equation (24) requires iterations, since $h_0 = h_0(x_1,x_2)$. For 2D flows, when $\delta/\delta x_3 \equiv 0$, operator (45) after multiplication by h_0^2 becomes separable, and the pressure equation may be solved by a fast direct cyclic reduction method [43].

To test the applicability of the method to elliptic coordinates a Lamb dipole flow was calculated with the similar parameters as in the previous section but in the elliptic computational domain $(x/2.6)^2 + (y/2.4)^2 \leqslant 1$. The computational mesh with 64×128 grid points and no ξ,η stretching ($\xi = x_1$, $\eta = x_2$) was used (shown in Fig. 5(a)).

Vorticity maps, corresponding to $t = 0$ and $t = 2$ are shown in Fig. 5(b) and (c). The evolution of the Lamb dipole does not indicate any distortion of the vortex due to the discretization. Distribution of the vorticity along the x-axis for $t = 2$ is given in Fig. 6 demonstrating absolutely smooth behaviour in all points including the neighbourhood of focuses at $x = \pm 1$.

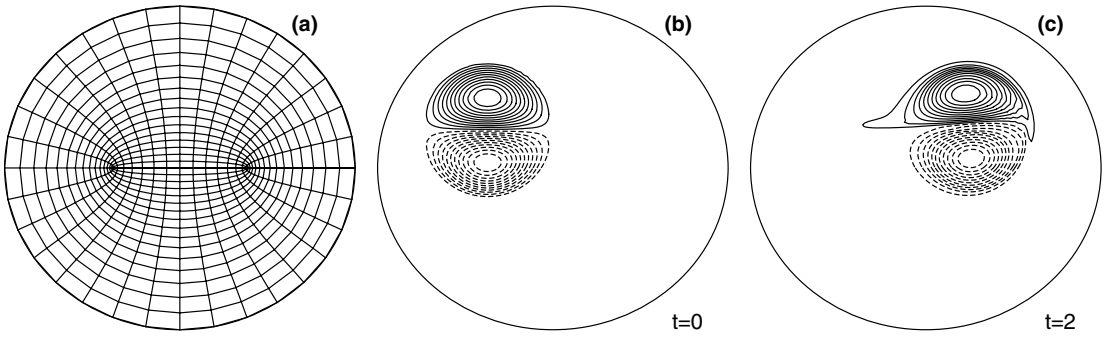

Fig. 5. Computational mesh (every 4th line in each direction is shown). Vorticity maps of the Lamb dipole at $t = 0$ and $t = 2$.

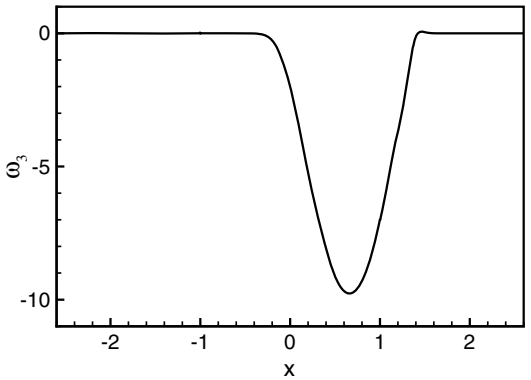

Fig. 6. Vorticity distribution along the line $y = 0$ at $t = 2$.

The results shown were obtained with the time-step $\Delta t = 1 \times 10^{-3}$ and the factorized viscous term (following from (33)–(35) with no modifications) as an implicit operator. The stability bound for this scheme was found to be $\Delta t \approx 3 \times 10^{-3}$. Note that the minimal grid spacing in the mesh was 3.16×10^{-4}, which is two times lesser than the minimal spacing in the cylindrical polar calculations. Thus, the stability restrictions in two coordinate systems look similar.

4.4. Spherical coordinates

Adaptation of the method to spherical coordinates is a straightforward. The pole problem is solved in a similar way as in cylindrical coordinates. As a test case of application of the method to spherical coordinates, consider a spherical Couette flow, i.e., the flow of incompressible fluid between two concentric spheres rotating about the same axis crossing their centers. The inner and outer radii of the spheres are R_1 and R_2, respectively. Ω_1 and Ω_2 are their angular velocities.

The computational coordinates $(x_1, x_2, x_3) = (\rho, \theta, \phi)$ are spherical polar coordinates with the axis of spheres rotation as a polar axis. The radial coordinate is stretched in order to obtain a nonuniform grid spacing

$$x = r \sin\theta \cos\phi, \quad y = r \sin\theta \sin\phi, \quad z = r \cos\theta, \quad r = r(\rho).$$

The corresponding metric stretching factors $(h_1, h_2, h_3) = (h_\rho, h_\theta, h_\phi)$ are

$$h_\rho(\rho) = r', \quad h_\theta(\rho) = r, \quad h_\phi(\rho, \theta) = r \sin\theta.$$

The discrete NSE look as follows:

$$\frac{\partial u_\rho}{\partial t} = \frac{1}{r\sin\theta}\overline{ru_\theta}^{\rho}\sin\theta\overline{\omega_\phi}^{\theta} - \frac{1}{r}\overline{ru_\phi}^{\rho}\overline{\omega_\theta}^{\phi} - \nu\frac{1}{r\sin\theta}\left(\frac{\delta\sin\theta\omega_\phi}{\delta\theta} - \frac{\delta\omega_\theta}{\delta\phi}\right) - \frac{1}{r'}\frac{\delta p}{\delta\rho}, \tag{46}$$

$$\frac{\partial u_\theta}{\partial t} = \overline{u_\phi}^{\theta}\overline{\omega_\rho}^{\phi} - \frac{1}{rr'}\overline{u_\rho}^{\theta}\overline{rr'\omega_\phi}^{\rho} - \nu\left(\frac{1}{r\sin\theta}\frac{\delta\omega_\rho}{\delta\phi} - \frac{1}{rr'}\frac{\delta r\omega_\phi}{\delta\rho}\right) - \frac{1}{r}\frac{\delta p}{\delta\theta}, \tag{47}$$

$$\frac{\partial u_\phi}{\partial t} = \frac{1}{rr'}\overline{u_\rho}^{\phi}\overline{rr'\omega_\theta}^{\rho} - \frac{1}{\sin\theta}\overline{u_\theta}^{\phi}\sin\theta\overline{\omega_\rho}^{\theta} - \nu\left(\frac{1}{rr'}\frac{\delta r\omega_\theta}{\delta\rho} - \frac{1}{r}\frac{\delta\omega_\rho}{\delta\theta}\right) - \frac{1}{r\sin\theta}\frac{\delta p}{\delta\phi}. \tag{48}$$

As in cylindrical coordinates, one pair of nonlinear terms in the NSE, namely the first term in (47) and the second term in (48), i.e., the terms containing ω_ρ are written in the form of (22), while the other two pairs are written in the regular form of (13)–(15). This is done to eliminate the need of u_θ at the polar axis. The boundary conditions follow from (18):

$$\begin{aligned} &u_\rho = \overline{ru_\theta}^{\rho} = 0, \quad \frac{1}{r}\overline{ru_\phi}^{\rho} = \Omega_1 R_1\sin\theta \quad \text{at } r = R_1,\\ &u_\rho = \overline{ru_\theta}^{\rho} = 0, \quad \frac{1}{r}\overline{ru_\phi}^{\rho} = \Omega_2 R_2\sin\theta \quad \text{at } r = R_2. \end{aligned} \tag{49}$$

The expressions for the continuity and vorticity equations as well as the expressions for the viscous term factorization follow directly from (16), (17), and (33)–(35) with no modifications.

The discrete Laplace operator in spherical coordinates has the following form:

$$\frac{1}{r^2 r'}\frac{\delta}{\delta\rho}\frac{r^2}{r'}\frac{\delta}{\delta\rho} + \frac{1}{r^2\sin\theta}\frac{\delta}{\delta\theta}\sin\theta\frac{\delta}{\delta\theta} + \frac{1}{r^2\sin^2\theta}\frac{\delta^2}{\delta\phi^2}. \tag{50}$$

The pressure equation (24) may be solved using FFT in the ϕ-direction and the cyclic reduction method [43] for the subsequent 2D Helmholtz equations.

Three dimensionless parameters completely define spherical Couette flow: two Reynolds numbers $Re_1 = \Omega_1 R_1^2/\nu$, $Re_2 = \Omega_2 R_2^2/\nu$, and the gap-size ratio $\delta = (R_2 - R_1)/R_1$. For the numerical test we selected the flow with $\delta = 1.27$ and $Re_2 = 0$, i.e., the large-gap flow with the inner sphere rotation only. It is known from experiments [44,45] and numerical simulations by a spectral method [46] that this flow being steady at low Reynolds number Re_1 becomes unsteady and three-dimensional at supercritical Reynolds numbers. The critical Reynolds number was estimated as $Re_c = 407$ in [44] and $Re_c = 406$ in [46]. In [45] was obtained $Re_c = 406$ for a slightly larger gap, $\delta = 1.33$. The first unstable mode corresponds to the azimuthal wavenumber $m = 3$, and the supercritical flows were described in [45,46] as laminar periodic flows with travelling waves in the azimuthal direction, antisymmetric with respect to the equator.

The computational mesh with $32 \times 128 \times 64$ grid nodes in the radial, meridional, and azimuthal directions, respectively, was used in the present simulations. At first, the flow at $Re_1 = 450$ was calculated. The initial conditions in this run were taken as a superposition of the axisymmetric Stokes flow velocity and some three-dimensional perturbation with the $\sim\exp(i\phi)$ azimuthal dependence. In Fig. 7(a) is shown time evolution of A_{3D}, the amplitude of 3D counterpart of the flow velocity

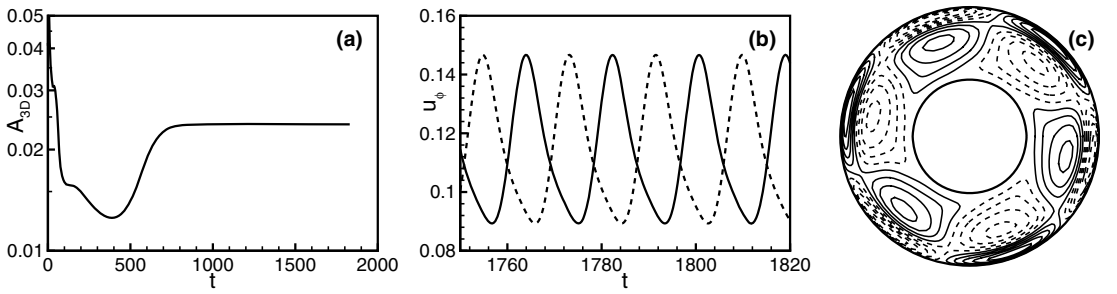

Fig. 7. Spherical Couette flow at $Re_1 = 450$, $Re_2 = 0$, $\delta = 1.27$. (a) Time-evolution of the amplitude of 3D velocity oscillations; (b) u_ϕ-velocity oscillations in two equatorially symmetric points: solid line, $(r,\theta,\phi) = (1.2,\pi/4,0)$, dashed line, $(1.2,3\pi/4,0)$; (c) u_θ distribution in the equatorial plane: solid lines – positive, dashed – negative values, $\Delta = \pm 0.01$. The velocity- and length-scales are $\Omega_1 R_1$ and R_1, respectively.

$$A_{3D}^2(t) = \frac{3}{4\pi(R_2^3 - R_1^3)} \int_0^{2\pi} \mathrm{d}\phi \int_0^{\pi} \mathrm{d}\theta \int_{R_1}^{R_2} |\mathbf{u}(t,r,\theta,\phi) - \mathbf{u}_{2D}(t,r,\theta)|^2 r^2 \sin\theta \,\mathrm{d}r,$$

where $\mathbf{u}_{2D}$ is the axisymmetric counterpart of the velocity

$$\mathbf{u}_{2D}(t,r,\theta) = \frac{1}{2\pi} \int_0^{2\pi} \mathbf{u}(t,r,\theta,\phi)\,\mathrm{d}\phi.$$

Fig. 7(a) shows that after a certain period of evolution the flow saturates finally on a constant-amplitude regime. The velocity oscillations in two equatorially symmetric points are presented in Fig. 7(b). Time periodicity of the oscillations with a 180°-phase shift between the two points is an evidence that the flow represents an equatorially antisymmetric travelling wave. Instantaneous u_θ distribution in the equatorial plane $\theta = \pi/2$ given in Fig. 7(c) demonstrates that the flow corresponds to the azimuthal wavenumber $m = 3$. All these observations agree with the experimental and numerical results of [44–46]. The period of velocity oscillation $T \approx 18\Omega_1^{-1}$ obtained in the present simulations coincides with that in simulations of [46] at slightly supercritical Reynolds number $Re_1 = 413$.

The flow at $Re_1 = 450$ was then used as an initial condition for simulations at smaller Reynolds numbers. Three-dimensional time-periodic regimes were observed down to $Re_1 = 410$, while at $Re_1 = 405$ the oscillations decayed and the flow eventually evolved to a 2D steady regime. The amplitude of 3D oscillations in the limiting regimes at different Reynolds numbers are given in Fig. 8. According to Landau theory [47], the amplitude of supercritical oscillations is proportional to $(Re_1 - Re_c)^{1/2}$, and our results conforms to this prediction. The critical Reynolds number, obtained by the extrapolation of the present results is $Re_c = 408$ which is in an excellent agreement with the cited experimental and numerical findings.

In closing, note, that the present simulations were performed with the time-step $\Delta t = 0.3\Omega_1^{-1}$. For the oscillations with a period $T \approx 18\Omega_1^{-1}$ this value looks quite reasonable.

4.5. Turbulent flow in annular eccentric pipe

Consider a pressure-gradient driven fluid flow along the gap between two parallel but eccentric cylinders of different radii, R_i and $R_o > R_i$ (see the sketch in Fig. 9(a)). If eccentricity e is comparable with the mean gap size $\delta = R_o - R_i$, then the width of the gap in the narrow part of the pipe $h = \delta - e$ will be considerably less than that in the wide part $H = \delta + e$. Consequently, the fluid velocity in the narrow gap will be less and the local Reynolds number will be significantly less than those in the wide gap. The geometrical parameters may be chosen in such a way that the local Reynolds number in the narrow gap will be too small to sustain turbulence, no matter how large is the global Reynolds number $Re = 2\delta U_b/\nu$ (here, 2δ is the hydraulic diameter and U_b is the bulk velocity). In the author's recent numerical study [14] it was indeed shown that two different flow regimes, namely fully turbulent and partly turbulent, may exist at the same Reynolds number $Re = 4000$ but different geometrical configurations (see Fig. 9(b) and (c)).

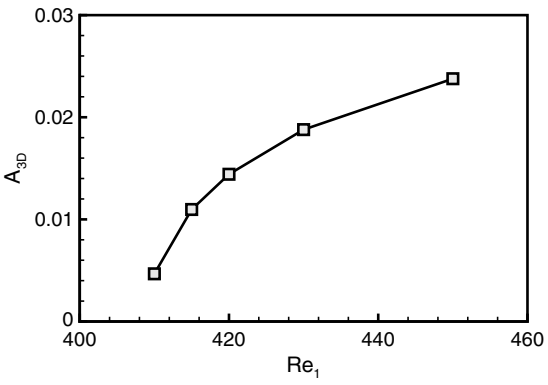

Fig. 8. Amplitude of 3D velocity oscillations at different supercritical Reynolds numbers.

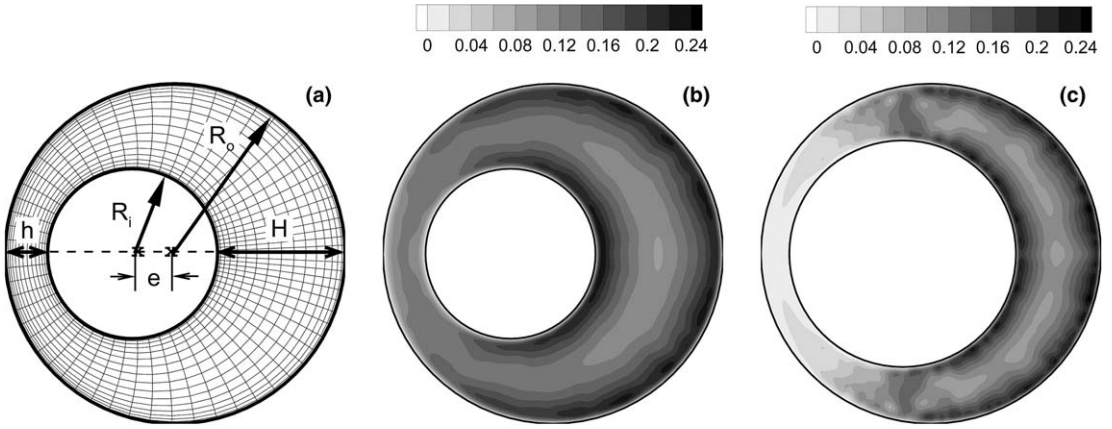

Fig. 9. (a) Sketch of the eccentric pipe's cross-section and computational mesh (every 4th line in each direction is shown). Contours of rms velocity fluctuations at $Re = 4000$ and $e/\delta = 0.5$ [14]: (b) fully turbulent flow ($\delta = R_i$); (c) partly turbulent flow ($\delta = R_i/2$). Velocity scale is the bulk velocity.

The flow in eccentric annular pipe is simulated with the use of bipolar coordinates (ξ, η) in the plane of the pipe's cross-section

$$x = -h_0(\xi,\eta)\sinh\xi, \quad y = h_0(\xi,\eta)\sin\eta, \quad h_0(\xi,\eta) = \frac{c}{\cosh\xi - \cos\eta} \tag{51}$$

with $c = [(R_o^2 - R_i^2 - e^2)^2/4e^2 - R_i^2]^{1/2}$. The new coordinates vary in the ranges $\eta \in [0,2\pi]$, $\xi \in [\xi_i, \xi_o]$, where $\xi_i = \ln[(1 + c^2/R_i^2)^{1/2} - c/R_i]$, $\xi_o = \ln[(1 + c^2/R_o^2)^{1/2} - c/R_o]$. The surface $\xi = \xi_i$ coincides with the inner cylinder, and the surface $\xi = \xi_o$ with the outer. The plane $\eta = 0$ intersects the pipe along the wide gap, and the plane $\eta = \pi$ along the narrow gap.

To get the node clustering in the dynamically active regions, namely in the near-wall regions and in the wide-gap part of the pipe the following coordinate stretching is used:

$$\xi = \alpha + \beta\tanh\gamma(x_1 - x_1^*), \quad x_1 \in [x_{1i}, x_{1o}] = [\xi_i, \xi_o],$$
$$\eta = x_2 - \lambda\sin x_2, \quad x_2 \in [0, 2\pi].$$

The constants α, β, γ, λ, and x_1^* are chosen reasoning from the desired mesh size in the physical space corresponding to the uniform grid in the computational space (x_1, x_2). The flow is homogeneous in the flow direction z, so the uniform grid is used in this direction. Coordinates $(x_1, x_2, x_3 = z)$ constitute an orthogonal system with the metric stretching factors

$$h_1(x_1,x_2) = h_0\xi'(x_1), \quad h_2(x_1,x_2) = h_0\eta'(x_2), \quad h_3 = 1$$

with $h_0(x_1, x_2)$ defined in (51).

The expressions for the discretized NSE, continuity and vorticity equations, as well as the expressions for the viscous term factorization follow directly from (13)–(17), and (33)–(35) with no modifications.

The discrete Laplace operator in bipolar cylindrical coordinates has exactly the same form as in the elliptic cylindrical coordinates (45). The only difference is in $h_0(x_1, x_2)$ function. In the 3D case the pressure equation cannot be solved by direct method. In the present simulations after FFT in the z-direction, it is solved iteratively using a combination of the cyclic reduction and the conjugate-gradient methods (for details see [14]).

Calculations were performed on the computational mesh with $64 \times 256 \times 64$ grid points and with the time-step of about $0.05\delta/U_b$. Two geometrical configurations: $(R_i, R_o, e) = (1, 2, 0.5)\delta$ and $(2, 3, 0.5)\delta$ at $Re = 4000$ were considered. Qualitatively different turbulent flow regimes were obtained in these two cases. In the first configuration turbulent fluctuations occupy all the pipe cross-section, while in the second configuration the region of turbulent flow coexists with the region of laminar flow. The rms velocity distributions in this two flows are shown in Fig. 9(b) and (c).

Eccentric annular pipe represents an ideal model for investigating inhomogeneous turbulent flow, where conditions of turbulence production vary significantly within the cross-section. It is also a convenient model

to study the peculiarities of the flow in the neighbourhood of the laminar/turbulent interface and the related entrainment phenomenon.

5. Summary

A finite-difference approach for the three-dimensional Navier–Stokes simulations in arbitrary curvilinear orthogonal coordinates is presented. It includes a new energy-conserving spatial discretization method and a semi-implicit third-order accurate Runge–Kutta scheme for time advancement. The time-advancement procedure exploits a convenient method for the implicit/explicit splitting when different terms of the NSE may be treated implicitly depending on the problem under consideration. In wall-bounded flows as well as in polar coordinates problems the most stiffness is usually produced by the viscous term of the NSE. A general algorithm for the viscous term decomposition with the aim of using the approximate factorization method is presented. A unified method for eliminating a so-called pole problem in polar coordinates is also provided. The robustness, accuracy, and stability of the method is tested thoroughly by simulating a number of laminar and turbulent flows in the Cartesian, cylindrical, spherical, elliptic, and bipolar coordinates. The method may be used for a wide range of laminar and turbulent flow simulations.

Acknowledgment

The research was supported by Russian Foundation for Basic Research under the Grant # 05-01-00607.

Appendix A. Third-order accuracy of time-integration scheme

The temporal third-order accuracy of the time integration scheme (27)–(30) is proved analytically and ascertained by analyzing both local and global errors in simulations of unsteady flows in a driven cavity in [35]. Here, the temporal accuracy of the scheme is evaluated considering turbulent pipe flow simulations of Section 4.2.1. The velocity field in a developed statistically steady-state is taken as an initial condition $\mathbf{u}(t_0)$. At first, the equations are integrated from t_0 to $t_1 = t_0 + 1$ by an explicit fourth-order Runge–Kutta method with the time-step $\Delta t = 5 \times 10^{-4}$ (time-scale is R/U_l, where R is the pipe radius and U_l is the laminar centerline velocity). This result is considered as "exact" solution $\mathbf{u}^{ex}(t_1)$. After that, starting from $\mathbf{u}(t_0)$ the approximate solutions $\mathbf{u}(t_1)$ are obtained with different $\Delta t \geqslant 2.5 \times 10^{-3}$ using the scheme (27)–(30), and the global errors are evaluated by comparison with the "exact" solution

$$\varepsilon = \max\{|u_i(t_1) - u_i^{ex}(t_1)|, \quad i = 1, 2, 3\}.$$

The maximum in the last formula is taken over all grid nodes. The dependence of the global error of time integration on the time-step size is shown in Fig. A.1. The $O(\Delta t^3)$ behaviour of $\varepsilon(\Delta t)$ supports the third-order accuracy of the scheme. Similar calculations were conducted using the low storage semi-implicit Runge–Kutta

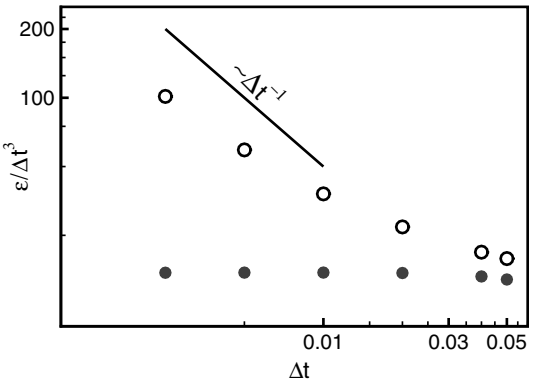

Fig. A.1. Global error of time integration as function of time-step size. Closed symbols, present scheme; open symbols, scheme [22].

scheme of [34] with coefficients used by Rai and Moin [33]. For application of the approximate factorization procedure a delta-form of the scheme, which can be found in [22], is used. Unlike the present scheme, $\varepsilon(\Delta t)$ for the scheme of [22,33,34] tends to a $O(\Delta t^2)$ behaviour at small Δt which reflects the second-order accuracy of this scheme.

Appendix B. Energy conservation by time-integration procedure

In order to demonstrate an energy-conservation property of the proposed method, numerical tests are conducted assuming an inviscid flow in a circular pipe. Even if the spatial discretization ideally satisfies the energy conservation, the energy may change due to the imperfectness of a time integration scheme. The initial velocity field is generated similarly to [27] by interpolating velocities from the fully developed turbulent pipe flow of Section 4.2.1 onto the $16 \times 16 \times 32$ mesh and normalizing the velocity to have zero mean velocity and unit specific kinetic energy $k = E/|D|$ (E is defined in (21), $|D|$ is the volume of computational domain).

It is known that explicit third-order accurate Runge–Kutta methods have a stability limit of CFL number $< \sqrt{3}$ when applying to the one-dimensional linear convection equation

$$\frac{\partial u}{\partial t} + c\frac{\partial u}{\partial x} = 0.$$

This is the reason of using third-order Runge–Kutta schemes for the nonlinear terms of the NSE rather than first- or second-order Runge–Kutta or Adams–Bashforth schemes, which are unconditionally unstable for the linear convection equation. It may be suspected that similar stability properties of time integration schemes are valid for the nonlinear inviscid equations. Fig. B.1 shows the evolution of kinetic energy for the inviscid flow simulations with different time-step sizes. For comparison the results of application the Adams–

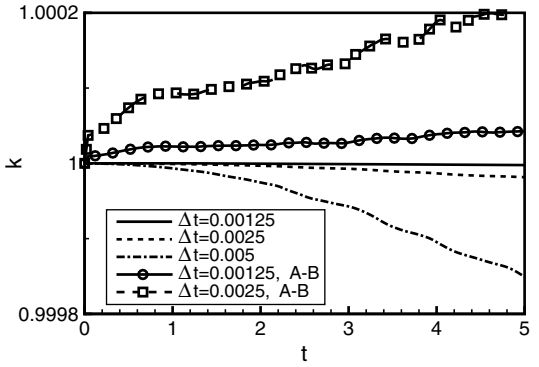

Fig. B.1. Kinetic energy evolution for inviscid flow in a pipe. Lines, present scheme; lines with symbols, Adams–Bashforth scheme.

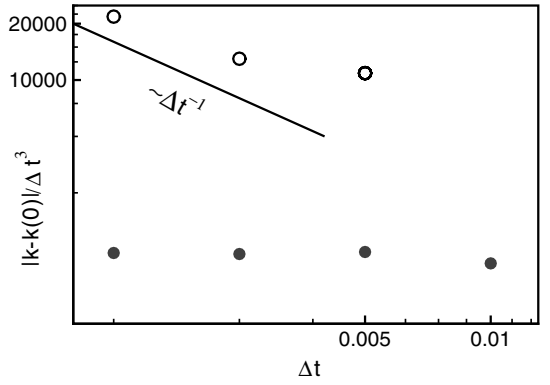

Fig. B.2. Kinetic energy error as function of a time-step size. Closed symbols, present scheme; open symbols, Adams–Bashforth scheme.

Bashforth scheme are also given in Fig. B.1. Peak CFL number over all grid points varies in this test flow in the range $40\Delta t$–$120\Delta t$. Runge–Kutta simulations are stable up to $\Delta t = 0.02$ which is in reasonable agreement with linear stability predictions. The energy in Runge–Kutta simulations with $\Delta t \leqslant 0.02$ slightly decreases with time due to the dissipative nature of third-order Runge–Kutta schemes. In contrast, simulations with the Adams–Bashforth scheme demonstrate gradual increase in $k(t)$ and diverge eventually for any Δt confirming the unconditional instability of this scheme.

The dependence of the kinetic energy error at the time moment $t = 5$ on the time-step size for the two tested schemes is shown in Fig. B.2. The error slope for small Δt is Δt^3 for the current scheme and Δt^2 for the Adams–Bashforth which is consistent with the orders of accuracy of both schemes.

References

[1] P. Moin, K. Mahesh, Direct numerical simulation: a tool in turbulence research, Annu. Rev. Fluid Mech. 30 (1998) 539.
[2] J. Jimenez, A. Pinelli, The autonomous cycle of near-wall turbulence, J. Fluid Mech. 389 (1999) 335.
[3] N.V. Nikitin, Turbulent channel flow with an artificial two-dimensional wall layer, Fluid Dyn. 38 (6) (2003) 854.
[4] R. Friedrich, T.J. Hüttl, M. Manhart, C. Wagner, Direct numerical simulation of incompressible turbulent flows, Comput. Fluids 30 (2001) 555.
[5] J. Kim, P. Moin, R. Moser, Turbulence statistics in fully developed channel flow at low Reynolds number, J. Fluid Mech. 177 (1987) 133.
[6] P.R. Spalart, Direct simulation of a turbulent boundary layer up to $Re_\theta = 1410$, J. Fluid Mech. 187 (1988) 61.
[7] J.G.M. Eggels, F. Unger, M.H. Weiss, J. Westerweel, R.J. Adrian, R. Friedrich, F.T.M. Nieuwstadt, Fully developed turbulent pipe flow: a comparison between direct numerical simulation and experiment, J. Fluid Mech. 268 (1994) 175.
[8] N.V. Nikitin, Direct numerical modelling of three-dimensional turbulent flows in pipes of circular cross section, Fluid Dyn. 29 (6) (1994) 749.
[9] N.V. Nikitin, Statistical characteristics of wall turbulence, Fluid Dyn. 31 (3) (1996) 361.
[10] S. Gavrilakis, Numerical simulation of low-Reynolds-number turbulent flow through a straight square duct, J. Fluid Mech. 244 (1992) 101.
[11] A. Huser, S. Biringen, Direct numerical simulation of turbulent flow in a square duct, J. Fluid Mech. 257 (1993) 65.
[12] N.V. Nikitin, Numerical simulation of turbulent flows in a pipe of square cross section, Physics-Doklady 42 (3) (1997) 158.
[13] N. Nikitin, A. Yakhot, Direct numerical simulation of turbulent flow in elliptical ducts, J. Fluid Mech. 532 (2005) 141.
[14] N.V. Nikitin, Direct simulation of turbulent flows in eccentric pipes, Comp. Math. Math. Phys. 46 (3) (2006).
[15] J.F. Thompson, Z.U.A. Warsi, C.W. Mastin, Numerical Grid Generation: Foundations and Applications, North-Holland, Amsterdam, 1985.
[16] J.E. Castilio (Ed.), Mathematical Aspects of Numerical Grid Generation, SIAM, Philadelphia, 1991.
[17] G. Iaccarino, R. Verzicco, Immersed boundary technique for turbulent flow simulations, Appl. Mech. Rev. 56 (2003) 331.
[18] E. Balaras, Modeling complex boundaries using an external force field on fixed Cartesian grids in large-eddy simulations, Comput. Fluids 33 (2004) 375.
[19] G. Williams, Numerical integration of the three-dimensional Navier–Stokes equations for incompressible flow, J. Fluid Mech. 37 (1969) 727.
[20] W. Huang, D. Sloan, Pole condition for singular problems: the pseudospectral approximation, J. Comput. Phys. 107 (1993) 254.
[21] N.V. Nikitin, A spectral finite-difference method of calculating turbulent flows of an incompressible fluid in pipes and channels, Comp. Math. Math. Phys. 34 (6) (1994) 785.
[22] R. Verzicco, P. Orlandi, A finite-difference scheme for the three-dimensional incompressible flows in cylindrical coordinates, J. Comput. Phys. 123 (1996) 402.
[23] K. Akselvoll, P. Moin, An efficient method for temporal integration of the Navier–Stokes equations in confined axisymmetric geometries, J. Comput. Phys. 125 (1996) 454.
[24] V. Priymak, T. Miyazaki, Accurate Navier–Stokes investigation of transitional and turbulent flows in a circular pipe, J. Comput. Phys. 142 (1998) 370.
[25] G. Constantinescu, S. Lele, A new method for accurate treatment of flow equations in cylindrical coordinates using series expansions, CTR Annu. Res. Briefs (2000) 199.
[26] K. Mohseni, T. Colonius, Numerical treatment of polar coordinate singularities, J. Comput. Phys. 157 (2000) 787.
[27] K. Fukagata, K.N. Kasagi, Highly energy-conservative finite difference method for the cylindrical coordinate system, J. Comput. Phys. 181 (2002) 478.
[28] Y. Morinishi, O. Vasilyev, T. Ogi, Fully conservative finite difference scheme in cylindrical coordinates for incompressible flow simulations, J. Comput. Phys. 197 (2004) 686.
[29] O. Zikanov, Symmetry-breaking bifurcations in spherical Couette flow, J. Fluid Mech. 310 (1996) 293.
[30] W. Sha, K. Nakabayashi, H. Ueda, An accurate second-order approximation factorization method for time-dependent incompressible Navier–Stokes equations in spherical polar coordinates, J. Comput. Phys. 142 (1998) 47.
[31] M. Oikawa, T. Karasudani, M. Funakoshi, Stability of flow between eccentric rotating cylinders, J. Phys. Soc. Jpn. 58 (1989) 2355.
[32] J. Kim, P. Moin, Application of a fractional-step method to incompressible Navier–Stokes equations, J. Comput. Phys. 59 (1985) 308.

[33] M.M. Rai, P. Moin, Direct simulations of turbulent flow using finite-difference schemes, J. Comput. Phys. 96 (1991) 15.
[34] P.R. Spalart, R.D. Moser, M. Rogers, Spectral methods for the Navier–Stokes equations with one infinite and two periodic directions, J. Comput. Phys. 96 (1991) 297.
[35] N. Nikitin, Third-order-accurate semi-implicit Runge–Kutta scheme for incompressible Navier–Stokes equations, Int. J. Numer. Meth. Fluids, DOI: 10.1002/fld.1122.
[36] D.L. Brown, R. Cortez, M.L. Minion, Accurate projection methods for the incompressible Navier–Stokes equations, J. Comput. Phys. 168 (2001) 464.
[37] J.K. Dukowicz, A.S. Dvinsky, Approximate factorization as a high order splitting for the implicit incompressible flow equations, J. Comput. Phys. 102 (1992) 336.
[38] J.B. Perot, An analysis of the fractional step method, J. Comput. Phys. 108 (1993) 51.
[39] F.H. Harlow, J.E. Welsh, Numerical calculation of time-dependent viscous incompressible flow with free surface, Phys. Fluids 8 (1965) 2182.
[40] H. Choi, P. Moin, Effects of the computational time step on numerical solutions of turbulent flow, J. Comput. Phys. 113 (1994) 1.
[41] F.E. Ham, F.S. Lien, A.B. Strong, A fully conservative second-order finite difference scheme for incompressible flow on nonuniform grids, J. Comput. Phys. 177 (2002) 117.
[42] K. Horiuti, DNS Database of Turbulence and Heat Transfer. Code number: CH12_PG.WL3. Available from: <http:/www.thtlab.t.u-tokyo.ac.jp/DNS/dns_database.html>.
[43] P.N. Swarztrauber, A direct method for the discrete solution of separable elliptic equations, SIAM J. Numer. Anal. 11 (1974) 1136.
[44] B.R. Munson, M. Menguturk, Viscous incompressible flow between concentric rotating spheres. Part 3. Linear stability and experiments, J. Fluid Mech. 69 (1975) 705.
[45] Y.N. Belyaev, A.A. Monakhov, I.M. Yavorskaya, Stability of spherical Couette flow in thick layers when the inner sphere revolves, Fluid Dyn. 13 (1975) 162.
[46] G. Dumas, Study of Spherical Couette Flow via 3-D Spectral Simulations: Large and Narrow-gap Flows and their Transitions, Ph.D. Thesis, California Institute of Technology, 1991.
[47] L.D. Landau, On the problem of turbulence, Doklady Akad. Nauk SSSR 44 (1944) 393 (in Russian). English translation in: D. Ter Haar (Ed.), Collected papers of L.D. Landau, Pergamon, Oxford, pp. 387–391.